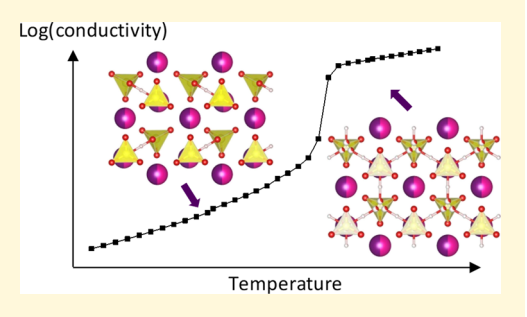


# Phase Behavior and Superionic Transport Characteristics of $(M_xRb_{1-x})_3H(SeO_4)_2$ (M = K or Cs) Solid Solutions

Dezhi Yi, †, \*\* Sheel Sanghvi, \*, \*\* Chatr Panithipongwut Kowalski, \*\* and Sossina M. Haile \*\*, \*, ||, |

Supporting Information

ABSTRACT: Solid acid selenates in the class  $M_3H(SeO_4)_2$ , in which M is an alkali ion, have garnered attention as a result of the dramatic increase in conductivity that occurs upon transition from a monoclinic to a superprotonic trigonal phase with a dynamically disordered hydrogen-bond network. The significant similarities between three specific members of this class, K<sub>3</sub>H(SeO<sub>4</sub>)<sub>2</sub>, Rb<sub>3</sub>H(SeO<sub>4</sub>)<sub>2</sub>, and Cs<sub>3</sub>H(SeO<sub>4</sub>)<sub>2</sub>, render the pseudobinary systems between end-members ideal for an exploration of the crystal chemical features that drive the superprotonic transition and control the magnitude of the conductivity. Accordingly, a systematic study of the  $(K_xRb_{1-x})_3H(SeO_4)_2$ and (Cs<sub>x</sub>Rb<sub>1-x</sub>)<sub>3</sub>H(SeO<sub>4</sub>)<sub>2</sub> systems is carried out here using in situ hightemperature diffraction and conductivity measurements by ac impedance



spectroscopy. Across the entire composition range, a transition to a superprotonic phase of the space group  $R\overline{3}m$  is observed. With decreasing average size of the alkali cation, the superprotonic transition temperature generally decreases and, for a given temperature, the conductivity monotonically increases. The variation in transition temperature with composition is discussed in terms of possible strain effects on the internal energy of the monoclinic phase. The conductivity in the superprotonic phase is found to obey the phenomenological compensation rule, in which the logarithm of the pre-exponential term is linearly correlated with the activation energy. The decrease in activation energy for proton transport with decreasing average cation size is tentatively ascribed to a contraction in the length of the hydrogen bonds, presumed from the contraction of the cell volume. Subtle changes in structure and conductivity occur at the special composition  $Cs_2RbH(SeO_4)_2$ , corresponding to a structure in which Cs and Rb species could be fully unmixed over available cation sites. While a fully ordered arrangement of cations was not observed, the larger cation was found to preferentially occupy the larger of the two cation sites in both high- and lowtemperature phases and in both chemical systems.

## 1. INTRODUCTION

The superprotonic transition that occurs in several solid acid compounds has garnered attention because of the spectacular 3-5 orders of magnitude jump in conductivity it induces. Tripotassium hydrogen diselenate,  $K_3H(SeO_4)_2$ , trirubidium hydrogen diselenate, Rb<sub>3</sub>H(SeO<sub>4</sub>)<sub>2</sub>, and tricesium hydrogen diselenate, Cs<sub>3</sub>H(SeO<sub>4</sub>)<sub>2</sub>, are superprotonic solid acids in the  $M_3H(XO_4)_2$  family, where  $M = NH_4$ , K, Rb, Cs and X = S, Se. K<sub>3</sub>H(SeO<sub>4</sub>)<sub>2</sub>, Rb<sub>3</sub>H(SeO<sub>4</sub>)<sub>2</sub>, and Cs<sub>3</sub>H(SeO<sub>4</sub>)<sub>2</sub> adopt monoclinic structures at ambient temperature and transform to a high conductivity, trigonal phase at slightly elevated temperatures similar to many other compounds in this group. Despite their global similarity, these compounds are structurally distinct at ambient temperature and show slightly different phase transition behavior.  $K_3H(SeO_4)_2$  and  $Rb_3H(SeO_4)_2$  have a monoclinic structure of space group A2/a under ambient conditions, and the former undergoes a direct transition to the superprotonic phase (space group  $R\overline{3}m$ ) at 115 °C. The latter, Rb<sub>3</sub>H(SeO<sub>4</sub>)<sub>2</sub>, transforms first to a second monoclinic phase (C2/m) at 175 °C, before transforming to the trigonal phase at

178 °C.<sup>2</sup> In contrast, Cs<sub>3</sub>H(SeO<sub>4</sub>)<sub>2</sub> adopts the C2/m monoclinic structure at room temperature, transforms to a phase with the A2/a monoclinic structure at 96 °C, and then further transforms to the superprotonic trigonal phase at 183 °C.<sup>3–8</sup> The sequence of transitions for the three compounds are thus

K<sub>3</sub>H(SeO<sub>4</sub>)<sub>2</sub>: 
$$A_{a}^{2}$$
  $\xrightarrow{115^{\circ}C}$   $\times R\overline{3}m$   
Rb<sub>3</sub>H(SeO<sub>4</sub>)<sub>2</sub>:  $A_{a}^{2}$   $\xrightarrow{175^{\circ}C}$   $\times C_{m}^{2}$   $\xrightarrow{178^{\circ}C}$   $\times R\overline{3}m$   
Cs<sub>3</sub>H(SeO<sub>4</sub>)<sub>2</sub>:  $C_{m}^{2}$   $\xrightarrow{96^{\circ}C}$   $\times A_{m}^{2}$   $\xrightarrow{183^{\circ}C}$   $\times R\overline{3}m$ 

where the respective A2/a, C2/m, and  $R\overline{3}m$  phases are essentially isostructural across the three systems. In addition to these high-temperature transformations, the  $M_3H(XO_4)_2$  class of compounds undergo ferroelectric transitions at low

Received: September 19, 2019 Revised: November 7, 2019 Published: November 7, 2019



<sup>&</sup>lt;sup>†</sup>Chemical Technology, East China University of Science and Technology, Shanghai 200237,China

<sup>&</sup>lt;sup>‡</sup>Department of Material Science and Engineering, <sup>∥</sup>Applied Physics, and <sup>⊥</sup>Department of Chemistry, Northwestern University, Evanston 60208, Illinois, United States

<sup>§</sup>Department of Materials Science, Faculty of Science, Chulalongkorn University, Bangkok 10330, Bangkok, Thailand

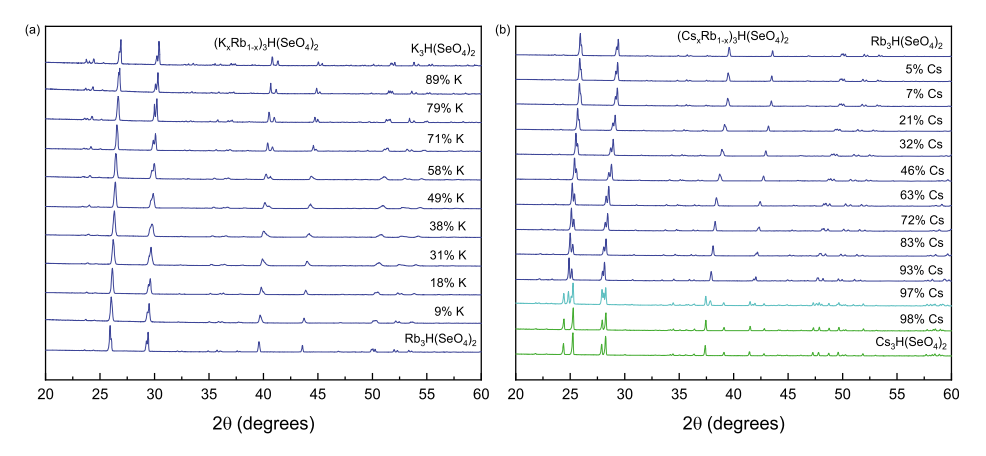


Figure 1. XRD patterns of  $(M_xRb_{1-x})_3H(SeO_4)_2$  (M = K or Cs) compositions at room temperature: (a)  $(K_xRb_{1-x})_3H(SeO_4)_2$  and (b)  $(Cs_xRb_{1-x})_3H(SeO_4)_2$ . Blue patterns correspond to the A2/a phase, green patterns to the C2/m phase, and aqua to a mixture of A2/a and C2/m phases.

temperatures, associated with the loss of inversion symmetry about hydrogen bonds. 9

The fascinating crystal chemistry of these materials has resulted in steady interest in their structural and transport properties. Based on the body of work accumulated over the past few decades, it is generally accepted that the high conductivity in the trigonal phase derives from the rotational disorder of the SeO<sub>4</sub> tetrahedral groups, which in turn supports dynamic disorder of the hydrogen-bond network. The entropy of the transition to the superprotonic phase, ranging in value from 6.7 to 9.4  $J/(mol \cdot K)$ ,  $^{10-13}$  has also been attributed to the configurational disorder. Specifically, in the trigonal phase, the apical oxygen atom of the single, crystallographically distinct SeO<sub>4</sub> group is dynamically disordered over three equivalent positions slightly displaced from the triad axis, given rise to a configurational entropy contribution to the total entropy of R  $\ln 3 = 9.13 \text{ J/(mol \cdot K)}$ . The high conductivity results from the dynamic rearrangement of the pairwise hydrogen-bond linkages between neighboring selenate groups. At room temperature, the structure is slightly distorted such that the tetrahedral groups are tilted along one of the three formerly equivalent directions. The hydrogen-bond positions become fixed, and the associated configurational entropy is zero. Thus, the observed transition entropy is largely accounted for in terms of these structure changes. The rather subtle nature of the structural changes that occur at the transition of  $K_3H(SeO_4)_2$ ,  $Rb_3H(SeO_4)_2$ , and  $Cs_3H(SeO_4)_2$  to their respective R3m phases further allows single-crystal samples to retain their morphological integrity. As a consequence, the high-temperature structures of these materials are well characterized. 14,15

The significant similarities between  $K_3H(SeO_4)_2$ ,  $Rb_3H(SeO_4)_2$ , and  $Cs_3H(SeO_4)_2$  at both low and high temperatures, and the high degree to which their properties are known render the pseudobinary systems between end-members ideal for an exploration of the crystal chemical features that drive the superprotonic transition and control the magnitude of the conductivity in the superprotonic phase. A wide range of cation sizes is systematically evaluated here, from  $K^+$  to  $Rb^+$  and then from  $Rb^+$  to  $Cs^+$ , by, respectively, examining the  $(K_xRb_{1-x})_3H-(SeO_4)_2$  and  $(Cs_xRb_{1-x})_3H(SeO_4)_2$  systems. Of particular interest is the possible connection between, on the one hand, cation site occupancies over the two crystallographically distinct cation sites of the A2/a, C2/m, and  $R\overline{3}m$  structures

and, on the other, transport properties. A recent study by Kiyanagi et al. has revealed that K and Rb preferentially occupy different sites in the A2/a room-temperature structure of the  $(K_xRb_{1-x})_3H(SeO_4)_2$  system, and the authors suggest the presence of a modulated superstructure. Whether the phenomena is specific to this chemical system, and how it may impact phase transition behavior is, as yet, unknown.

## 2. METHODS

Full details of the experimental methods are available in the Supporting Information. In brief, materials of composition  $(K_xRb_{1-x})_3H(SeO_4)_2$  and  $(Cs_xRb_{1-x})_3H(SeO_4)_2$  in approximate x increments of 0.1 were synthesized via a combination of precipitation and solid-state techniques. Compositions of the prepared materials were measured using energy-dispersive X-ray spectroscopy (EDS) in conjunction with scanning electron microscopy. In all cases, results are reported with respect to the measured composition, which occasionally varied slightly from the nominal (Figure S1).

Phase analysis was performed by powder X-ray diffraction (XRD). Ambient temperature powder diffraction data were collected using a STOE STADI P diffractometer using acquisition parameters suitable for refinement of crystallographic data. High-temperature diffraction data were collected in situ, using an integrated high-temperature stage (either Anton Paar HT1200 or HTK1500). The atmosphere was humidified with an H<sub>2</sub>O partial pressure of ~0.023 atm (balance either He or N2) to suppress dehydration. Diffraction patterns were collected at temperatures in the vicinity of what was identified as the transition to the trigonal phase after ~15 min of thermal equilibration after each heating step. In some cases, a temperature step as small as 1 °C was utilized to capture the full features of the phase transition behavior, but a step of 5 °C was more typical. All compositions in the  $(Cs_xRb_{1-x})_3H(SeO_4)_2$  system and a representative subset of those in the  $(K_xRb_{1-x})_3H(SeO_4)_2$  were studied at high temperatures. Diffraction data were analyzed by Rietveld refinement using the software package GSAS.<sup>17</sup> Refinements were carried out under the constraint that the overall composition reflects that measured by EDS. Full details of the refinement procedures are provided in the Supporting Information (Table S1).

Conductivity was measured by ac impedance spectroscopy using uniaxially pressed polycrystalline compacts. For reasons of convenience, colloidal silver paste was used at the electrode material for compositions in the  $(K_xRb_{1-x})_3H(SeO_4)_2$  system, whereas sputtered Pt was used for those in the  $(Cs_xRb_{1-x})_3H(SeO_4)_2$  system. The maximum temperature of the experiments was set to capture but not greatly exceed, the transition, with measurements made in temperature steps of  $\sim 2$  °C. Impedance data were collected over the frequency range of 0.1 Hz and 100 kHz using a voltage amplitude of

20 mV, after a thermal equilibration of  $\sim$ 15 min. The  $H_2O$  partial pressure was maintained at  $\sim$  0.47 atm (balance  $N_2$ ).

## 3. RESULTS AND DISCUSSION

3.1. Structural Properties. The diffraction studies revealed that  $K_3H(SeO_4)_2$  and  $Rb_3H(SeO_4)_2$  are completely miscible at room temperature, Figure 1a. All compositions in this system crystallize with the monoclinic structure in space group A2/a. The results are consistent with what has been previously reported by Kiyanagi et al. for the specific intermediate compositions K2RbH(SeO4)2 and KRb2H- $(SeO_4)_2$ . In the  $(Cs_xRb_{1-x})_3H(SeO_4)_2$  system, the distinct structures of the end-members preclude complete miscibility at ambient temperature. The results, Figure 1b, reveal high solubility of Cs into  $Rb_3H(SeO_4)_2$ , with the A2/a monoclinic phase observed up to 93 at. %. Conversely, the solubility of Rb into the C2/m structure of  $Cs_3H(SeO_4)_2$  is only  $\sim 2$  at. %. At 97% Cs, a two-phase mixture of both the Rb<sub>3</sub>H(SeO<sub>4</sub>)<sub>2</sub> and Cs<sub>3</sub>H(SeO<sub>4</sub>)<sub>2</sub> structure types occurs. The crystallographic parameters (atomic coordinates and equivalent isotropic displacement parameter) extracted from Rietveld analysis of the three end-members patterns are reported in Tables 1-3. Selected parameters of the solid solution compositions are presented in Tables 4 and S3.

Table 1. Atomic Coordinates and Isotropic Displacement Parameters in  $K_3H(SeO_4)_2$  at Room Temperature, Refined in Space Group A2/a with a = 10.1388(12) Å, b = 5.9074(5) Å, c = 14.9701(2) Å, and  $\beta = 103.649(3)^{\circ a,b}$ 

atom	site	$\boldsymbol{x}$	у	z	$U_{\rm iso}~({\rm \AA}^2)$
K(1)	4e	0.25	0.757(2)	0	0.009(2)
K(2)	8f	0.6511(5)	0.733(2)	0.1965(3)	0.013(2)
Se	8f	0.4599(3)	0.2317(6)	0.11706(14)	0.0013(4)
O(1)	8f	0.397(2)	0.021(3)	0.1614(8)	0.0040(4)
O(2)	8f	0.4341(11)	0.184(2)	0.0039(6)	0.0040(4)
O(3)	8f	0.6247(10)	0.239(3)	0.1532(6)	0.0040(4)
O(4)	8f	0.385(2)	0.472(2)	0.1317(9)	0.0040(4)
Н	4a	0.5000	0.0000	0.0000	

<sup>a</sup>All atom sites are fully occupied.  $R_{\rm exp}=3.22\%$  and  $R_{\rm wp}=5.68\%$ . <sup>b</sup>fixed at 1/3  $U_{\rm iso}$  of oxygen atoms to avoid falling below zero; ratio selected based on results of refinement of Rb and Cs structures.

Upon heating, all compositions displayed a transition to the  $R\overline{3}m$  trigonal phase; a selection of high-temperature diffraction data presented in Figure 2. Thus, complete solid-solubility is displayed in both the  $(K_xRb_{1-x})_3H(SeO_4)_2$  and  $(Cs_xRb_{1-x})_3H(SeO_4)_2$  systems at high temperatures, in addition to the high

Table 3. Atomic Coordinates and Isotropic Displacement Parameters in  $Cs_3H(SeO_4)_2$  at Room Temperature, Refined in Space Group C2/m with a = 10.901(2) Å, b = 6.3911(3) Å, c = 8.4484(12) Å, and  $\beta = 112.443(3)^{\circ a}$ 

atom	site	x	у	z	$U_{\rm iso}~({\rm \AA}^2)$
Cs(1)	2a	0	0	0	0.0152(12)
Cs(2)	4i	0.1977(2)	0	0.6075(3)	0.0185(9)
Se	4i	0.4281(3)	0	0.2368(4)	0.0117(14)
O(1)	8j	0.4819(9)	0.217(2)	0.6846(11)	0.031(3)
O(2)	4i	0.3825(12)	0	0.022(2)	0.031(3)
O(3)	4i	0.2885(14)	0	0.269(2)	0.031(3)
Н	2b	0.5000	0.0000	0.0000	

<sup>a</sup>All atom sites are fully occupied.  $R_{\text{exp}} = 3.61\%$  and  $R_{\text{wp}} = 4.90\%$ .

miscibility at room temperature. From the structural refinements based on these data, several trends emerge (Table 5). The molar volumes of both monoclinic phases (A2/a and C2/a)m) and the trigonal phase increase monotonically with increasing effective cation radius, as would be expected, Figure 3. In the crystal with 97% Cs, the C2/m structure supports a more compact arrangement than the A2/m does (Figure 2b), reflected in the abrupt decrease in cell volume at this composition. In the  $(K_xRb_{1-x})_3H(SeO_4)_2$  system, the hightemperature molar volumes are reported for measurements at different temperatures as a consequence of the differing transition temperatures and unknown high-temperature thermal stability (Figure 2). Consequently, the results are convoluted with thermal expansion effects. However, it can be concluded that the chemical effects are dominant. A molar volume difference between K<sub>3</sub>H(SeO<sub>4</sub>)<sub>2</sub> and Rb<sub>3</sub>H(SeO<sub>4</sub>)<sub>2</sub> of 9% is observed, of which only a small fraction can be due to thermal expansion between 115 and 190 °C, the respective measurement temperatures.

Far more significant than the molar volume trends, which essentially follow Vegard's Law, <sup>18</sup> are a measurable preference of the cations for distinct sites. All three structure types of this study  $(A2/m, C2/m \ and \ R3m)$  have two crystallographically distinct cation sites (Figure 4). The first site is generically designated here as the M(1) site, and it appears at Wyckoff position 4e in the A2/a structure, 2a in the C2/m structure, and 3a in the R33m structure. The second, M(2), appears at Wyckoff positions 8f, 4i, and 6c, respectively, in the three structures. The Se atom, and thus the entire selenate group, is located in a single crystallographic site in all three structures. In both the  $(K_xRb_{1-x})_3H(SeO_4)_2$  and  $(Cs_xRb_{1-x})_3H(SeO_4)_2$  systems, and consistent with that reported by Kiyanagi et al., <sup>16</sup> the larger cation preferentially occupies the M(2) site,

Table 2. Atomic Coordinates and Isotropic Displacement Parameters in Rb<sub>3</sub>H(SeO<sub>4</sub>)<sub>2</sub> at Room Temperature, Refined in Space Group A2/a with a = 10.4899(8) Å, b = 6.0985(3) Å, c = 15.4458(13) Å, and  $\beta = 102.910(3)^{\circ a}$ 

atom	site	$\boldsymbol{x}$	y	z	$U_{\rm iso}~({ m \AA}^2)$
Rb(1)	4e	0.25	0.7533(8)	0	0.0093(10)
Rb(2)	8f	0.6510(3)	0.7329(6)	0.19532(12)	0.0159(7)
Se	8f	0.4611(3)	0.2253(5)	0.11670(10)	0.0080(9)
O(1)	8f	0.3911(15)	0.013(2)	0.1597(8)	0.022(2)
O(2)	8f	0.4444(10)	0.188(2)	0.0062(5)	0.022(2)
O(3)	8f	0.6194(10)	0.247(2)	0.1541(6)	0.022(2)
O(4)	8f	0.3869(15)	0.460(2)	0.1284(8)	0.022(2)
Н	4a	0.0000	0.0000	0.0000	

<sup>&</sup>lt;sup>a</sup>All atom sites are fully occupied.  $R_{\text{exp}} = 2.94\%$  and  $R_{\text{wp}} = 3.69\%$ .

Table 4. Selected Refinement Parameters, Space Groups, Refined Lattice Parameters, and Refined Site Occupancies of  $(K_xRb_{1-x})_3H(SeO_4)_2$  and  $(Cs_xRb_{1-x})_3H(SeO_4)_2$  Solid Solutions at Room Temperature<sup>a</sup>

R-values				lattice parameters				site occupancy by Rb	
% K measured	R <sub>exp</sub> (%)	R <sub>wp</sub> (%)	space group	a (Å)	b (Å)	c (Å)	$\beta$ (deg)	M(1)	M(2)
100	3.22	5.68	A2/a	10.1388(12)	5.9074(5)	14.9701(2)	103.649(3)	0	0
89(1)	2.16	3.70	A2/a	10.1828(2)	5.9352(1)	15.0328(4)	103.595(1)	0.03(1)	0.15(1)
79(1)	2.26	4.99	A2/a	10.2172(2)	5.9556(1)	15.0814(5)	103.546(1)	0.18(1)	0.22(1)
71(1)	2.28	5.28	A2/a	10.2561(3)	5.9762(1)	15.1297(6)	103.497(1)	0.08(1)	0.39(1)
58(2)	2.21	5.57	A2/a	10.2939(6)	5.9978(1)	15.1862(11)	103.436(3)	0.12(1)	0.57(1)
48(2)	2.31	7.88	A2/a	10.3266(8)	6.0112(2)	15.2196(15)	103.387(4)	0.28(1)	0.64(1)
38(1)	2.24	6.86	A2/a	10.3566(9)	6.0288(2)	15.253(2)	103.204(5)	0.28(1)	0.79(1)
31(2)	2.27	6.12	A2/a	10.3925(7)	6.0460(2)	15.3036(14)	103.118(4)	0.41(1)	0.83(1)
18(1)	2.27	4.96	A2/a	10.4228(4)	6.0649(1)	15.3557(7)	103.092(2)	0.46	1.00
9(1)	2.20	3.51	A2/a	10.4587(3)	6.0835(1)	15.4034(5)	102.995(1)	0.73	1.00
0	2.94	3.69	A2/a	10.4899(8)	6.0985(3)	15.4458(13)	102.910(3)	1	1
	R-values			lattice parameters				site occupancy by Cs	
% Cs measured	R <sub>exp</sub> (%)	R <sub>wp</sub> (%)	space group	a (Å)	b (Å)	c (Å)	$\beta$ (deg)	M(1)	M(2)
0	2.94	3.69	A2/a	10.4899(8)	6.0985(3)	15.4458(13)	102.910(3)	0	0
5(1)	1.96	3.70	A2/a	10.5116(9)	6.1149(4)	15.475(2)	102.920(2)	0.02(1)	0.07(1)
7(1)	1.97	3.29	A2/a	10.5237(11)	6.1231(5)	15.491(2)	102.925(2)	0.08(1)	0.06(1)
21(2)	2.06	3.34	A2/a	10.5898(14)	6.1708(6)	15.577(2)	102.924(3)	0.21(1)	0.21(1)
32(2)	2.09	3.70	A2/a	10.6461(14)	6.2095(6)	15.651(2)	102.904(3)	0.22(2)	0.37(1)
46(2)	2.14	3.81	A2/a	10.7062(15)	6.2484(6)	15.725(3)	102.864(3)	0.23(2)	0.57(1)
63(1)	2.23	3.81	A2/a	10.7922(14)	6.3004(6)	15.825(2)	102.796(3)	0.27(2)	0.81(1)
72(2)	2.39	3.85	A2/a	10.8329(12)	6.3198(5)	15.862(2)	102.752(3)	0.40(2)	0.88(1)
83(1)	2.24	4.43	A2/a	10.8878(12)	6.3467(5)	15.912(2)	102.693(3)	0.49	1.00
93(2)	2.46	3.94	A2/a	10.9399(12)	6.3705(5)	15.958(2)	102.647(2)	0.79	1.00
97(1)	2.41	3.75	A2/a	10.9717(8)	6.3859(3)	15.9918(14)	102.640(2)	0.90	1.00
			C2/m	10.895(2)	6.3783(3)	8.4430(13)	112.541(3)	0.90	1.00
98(1)	2.93	4.47	C2/m	10.8951(15)	6.3804(2)	8.4424(10)	112.511(2)	0.93	1.00
100	3.61	4.90	C2/m	10.901(2)	6.3911(3)	8.4484(12)	112.443(3)	1	1

<sup>&</sup>quot;Occupancies which refined to values >1 were fixed to 1.00, implying a fixed occupancy value on the remaining cation site to match the measured composition.

irrespective of the phase, Figure 5, that is, as the larger cation is introduced into the solid solutions, it is incorporated primarily on the M(2) site. Only after the M(2) site is fully occupied by the larger cation does substantial incorporation occur on the M(1) site. The composition M'M2"H(SeO4)2 can be considered a special composition reflecting a structure in which the larger M'' cation entirely occupies the M(2) site and the smaller M' cation entirely occupies the M(1) site. While the data do not reveal such perfect site ordering, it is noted that because of the platelet morphology of the crystallites, preferred orientation effects complicated the refinement. Such effects were particularly severe in the high-temperature measurements because the samples could not be spun during data collection because of the geometry of the heating stage. Thus, the statistical uncertainty implied by the refinements most certainly underestimates the true uncertainty, and the extent of site disproportionation is not fully known.

The origin of the site occupancy trends can be rationalized in terms of the crystal structures. As shown in Figure 4, the  $M_3H(SeO_4)_2$  structures are comprised of double layers of hydrogen-bond-linked  $SeO_4$  groups. Hydrogen bonds form between the apical oxygen atoms of the selenate groups, and in the trigonal phase, the hydrogen bond is dynamically distributed between three possible directions. The M(1) cation sites lie in the interstices of the  $H(SeO_4)_2$  layers, coordinated by six oxygen neighbors (none of which participates in hydrogen bonding). The M(2) cations reside

between the H(SeO<sub>4</sub>)<sub>2</sub> layers, coordinated by ten oxygen neighbors (with one participating in hydrogen-bond formation). The polyhedra about M(1) are substantially smaller than those about M(2). For example, in  $Rb_3H(SeO_4)_2$ , the M(1)-O distances range from 2.813(13) to 3.026(13) Å (Table S2) with an average of 2.946(11) Å, whereas the M(2)-Odistances range from 2.881(12) to 3.40(4) Å, with an average value of 3.107 Å. The larger cation is thus incorporated into the M site with a larger coordination polyhedron, the M(2)site. It might also be expected that preferential incorporation of the larger cation into the site between the (001) aligned  $H(SeO_4)_2$  bilayers would expand the lattice normal to (001) more than in the (001) plane. However, the chemically induced expansion is isotropic in the  $(K_xRb_{1-x})_3H(SeO_4)_2$ system and in fact is slightly greater within the (001) plane than normal to it in the  $(C_xRb_{1-x})_3H(SeO_4)_2$  system (Figure S3). Moreover, much like the overall molar volume at room temperature (Figure 3a,b), the anisotropic chemical expansion is approximately linear with composition. Thus, the site occupancy preferences have no unusual influence on the cell dimensions.

Consideration of the interatomic distances, in contrast, reveals a possible impact of the cation site disproportionation. In the trigonal phase, the M(2) atom, the apical oxygen, and the Se are all aligned along the three-fold axis (not shown). In the monoclinic structures, this alignment is largely retained and the M(2) atoms are located almost directly above the apical

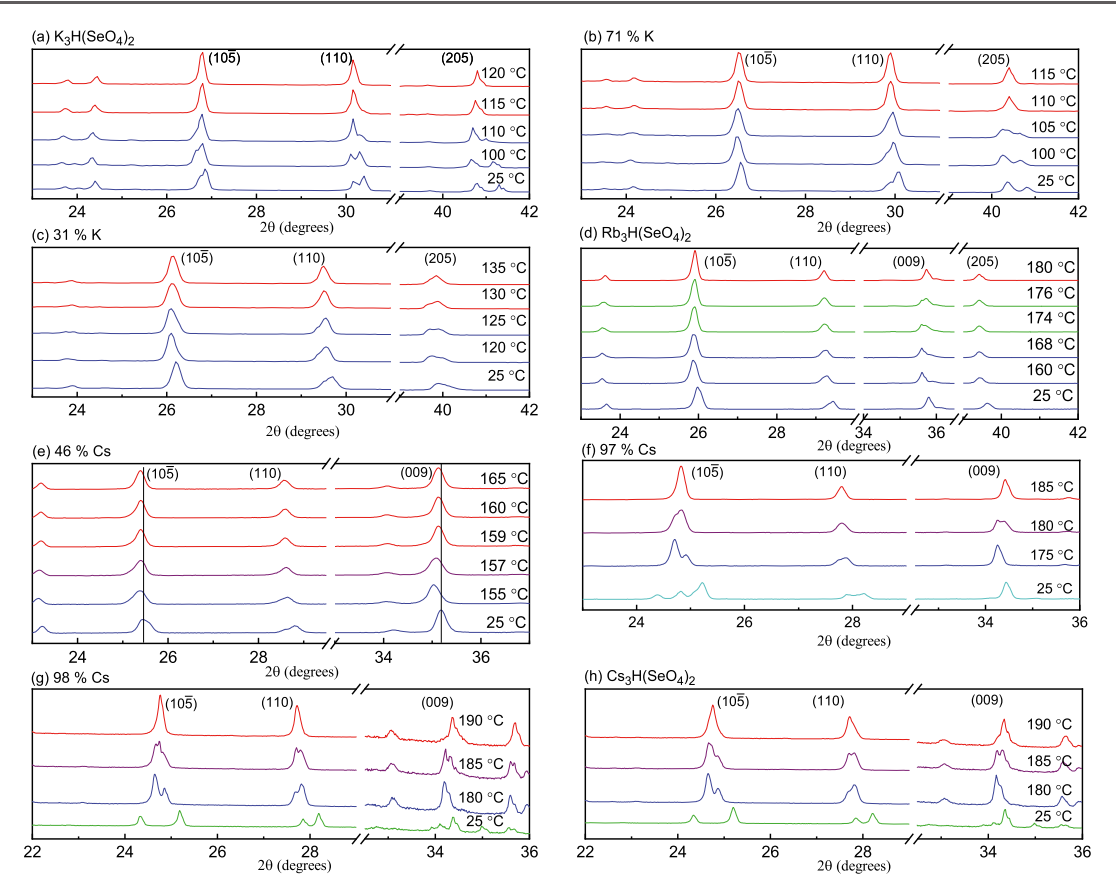


Figure 2. HT-XRD patterns at indicated temperatures under lightly humidified nitrogen or helium  $(pH_2O \approx 0.023 \text{ atm})$  of compositions in the  $(M_xRb_{1-x})_3H(SeO_4)_2$  (M = K or Cs) systems: (a)  $K_3H(SeO_4)_2$  (b) 71% K, (c) 31% K, (d)  $Rb_3H(SeO_4)_2$ , (e) 46% Cs, (f) 97% Cs, (g) 98% Cs, and (h)  $Cs_3H(SeO_4)_2$ . Blue patterns correspond to the A2/a phase, green patterns to the C2/m phase, aqua patterns to a mixture of A2/a and C2/m phases, and red patterns to the R3m phase. The vertical lines in (e) are guides to the eye intended to highlight the small peak shifts.

oxygen atoms and Se atoms along the  $c^*$  direction, Figures 4a,b. The M(2)–Se distance along this pseudotrigonal axis, Figure 6, increases almost linearly in the  $(K_xRb_{1-x})_3H(SeO_4)_2$  system. In the case of the  $(C_xRb_{1-x})_3H(SeO_4)_2$  system, however, there is a distinct change in the slope at the special composition  $RbCs_2H(SeO_4)_2$ . Because the distance between planes does not show a similar change in the slope (Figure S3), the behavior suggests a change in the selenate group orientation and/or geometry upon incorporation of Cs into M(1). The structural distortion is apparently too severe to accommodate a Cs concentration of greater than ~90% on this site, driving the transition of  $Cs_3H(SeO_4)_2$  at ambient conditions to the C2/m structure.

**3.2. Phase Behavior.** The conductivity measurements, Figure 7, revealed that all compositions displayed a transition to a superprotonic phase, with the onset to the sharp conductivity regime defined here as the transition temperature,  $T_{\rm sp}$ . The diffraction and impedance data were combined to develop the phase diagrams of the  $(K_xRb_{1-x})_3H(SeO_4)_2$  and  $(Cs_xRb_{1-x})_3H(SeO_4)_2$  systems presented in Figure 8. Comparison to the temperature at which the conductivity reflected a complete transformation to the superprotonic state is provided in the Supporting Information (Figure S4). For reference, vertical lines representing special compositions  $KRb_2H(SeO_4)_2$  and  $RbCs_2H(SeO_4)_2$  are indicated on the phase diagrams. Dehydration behavior was not quantitatively studied here, but overall, the thermal stability of the  $(K_xRb_{1-x})_3H(SeO_4)_2$  system was found to be lower than that of  $(Cs_xRb_{1-x})_3H$ .

 $(SeO_4)_2$ . The highest temperatures of the conductivity measurements, which represent the lower limit on the thermal stability of the  $R\overline{3}m$  phase under  $pH_2O = 0.47$  atm, are reported in Figure S4.

The phase transformations measured here for the endmember materials are consistent with the reported literature. In particular,  $K_3H(SeO_4)_2$  transforms from the room temperature A2/a phase to the  $R\overline{3}m$  phase between 110 and 115 °C as determined by diffraction, Figure 2a, and at 113 °C as determined by the onset of the high conductivity behavior. The changes in diffraction features between the 110 and 115 °C spectra are subtle, just as the physical changes to the structure are subtle, but they are nevertheless detectable. In the case of Rb<sub>3</sub>H(SeO<sub>4</sub>)<sub>2</sub>, the intermediate phase of space group C2/m, identified at 174 and 176 °C, Figure 2d, is not immediately evident from the peak splitting; however, its presence was supported on the basis of lattice parameter refinements. The corresponding conductivity data revealed the transition to the R3m phase at 179 °C. The  $Cs_3H(SeO_4)_2$ compound clearly shows the presence of the expected A2/a phase at 180 °C which completely transforms to the  $R\overline{3}m$ phase by 190 °C, Figure 2h. Generally consistent with these results, the onset to high conductivity in  $Cs_3H(SeO_4)_2$  occurs

In several of the intermediate compositions, the phase transformations were similarly subtle, particularly in the  $(K_xRb_{1-x})_3H(SeO_4)_2$  system. Nevertheless, the transition behavior was detectable. In Figure 2a–d, the raw diffraction

Table 5. Lattice Parameters in the  $R\overline{3}m$  Phase of  $(K_xRb_{1-x})_3H(SeO_4)_2$  and  $(Cs_xRb_{1-x})_3H(SeO_4)_2$  Solid Solutions at the Temperature Indicated

	R-values			lattice parameters		
% K measured	R <sub>exp</sub> (%)	R <sub>wp</sub> (%)	T, °C	a (Å)	c (Å)	
100	3.33	13.03	115	5.9104(7)	21.809(2)	
71(1)	3.40	12.47	115	5.9689(9)	22.044(2)	
58(2)	3.22	12.77	120	5.9873(11)	22.113(3)	
38(1)	1.34	10.90	130	6.0373(9)	22.370(2)	
31(2)	1.97	9.96	130	6.0417(5)	22.3842(13)	
9(1)	3.14	15.38	165	6.0848(12)	22.601(3)	
0	3.78	15.59	190	6.1133(5)	22.5917(10)	
	R-values			lattice p	arameters	
% Cs measured	R <sub>exp</sub> (%)	R <sub>wp</sub> (%)	T, °C	a (Å)	c (Å)	
0	3.78	15.59	190	6.1133(5)	22.5917(10)	
5(1)	2.09	4.23	190	6.1257(4)	22.6600(11)	
7(1)	2.11	4.81	190	6.1297(5)	22.6592(13)	
21(2)	1.90	6.58	190	6.1578(6)	22.7403(11)	
32(2)	2.19	5.96	190	6.2010(8)	22.876(2)	
46(2)	2.28	6.70	190	6.2451(6)	22.9721(13)	
63(1)	2.34	8.48	190	6.2884(8)	23.114(2)	
72(2)	2.40	9.92	190	6.3134(7)	23.1842(15)	
83(1)	2.83	11.42	190	6.3520(9)	23.2672(15)	
93(2)	2.85	10.85	190	6.3837(8)	23.3446(15)	
97(1)	2.82	11.01	190	6.4012(8)	23.3871(15)	
98(1)	2.10	4.81	190	6.4121(6)	23.489(2)	
100	2.00	8.69	190	6.4183(12)	23.429(4)	

patterns reveal splitting of what correspond to the  $(1 \ 0 \ -5)$ ,  $(1 \$ 1 0), and (2 0 5) peaks of the hexagonal unit cell when the monoclinic phase is present that disappear when only the trigonal phase occurs. In the Cs-rich (Cs<sub>x</sub>Rb<sub>1-x</sub>)<sub>3</sub>H(SeO<sub>4</sub>)<sub>2</sub> materials, clearer distinction between phases was evident, as shown, for example, in Figure 2f, in which the split of the hexagonal  $(1 \ 0 \ -5)$  phase is strong at room temperature. In the Rb-rich compositions of this system, the transformation was reflected not by the merging of peaks but rather by an unusual thermal contraction in the [0 0 1] direction. This behavior is evident, for example, in the composition with 46 at. % Cs, Figure 2e, in which the (0 0 9) peak shifts to an increasingly high angle between 155 and 159 °C. The coexistence of phases at 157 °C is concluded from the breadth of the diffraction peaks. As indicated in Figure 2, the coexistence of two phases was in fact rarely detected. While higher resolution and higher sensitivity would be required to definitely map out the two-phase regions, the diffraction results nevertheless indicate that such regions are rather narrow. This is corroborated by the relatively narrow temperature range over which the conductivity increases, Figures 7 and S4.

The phase behavior in both systems is thus described as approximately isomorphous with a weakly composition-dependent transition temperature. The narrow extent of two-phase regions implies that the cation mixing thermodynamics are similar in the high- and low-temperature phases. Analogous behavior has been observed in the  $CsH_2PO_4-RbH_2PO_4$  system. Both the  $(K_xRb_{1-x})_3H(SeO_4)_2$  and  $(Cs_xRb_{1-x})_3H-(SeO_4)_2$  systems furthermore display a minimum transition temperature at an intermediate composition: at 79 at. K in the  $(K_xRb_{1-x})_3H(SeO_4)_2$  system and at 46 at. Cs in the  $(Cs_xRb_{1-x})_3H(SeO_4)_2$  system. Both phase diagrams also have a small peritectiod region near  $Rb_3H(SeO_4)_2$ , reflecting the

occurrence of the C2/m phase at high temperatures in the Rb compound. Perhaps surprisingly, the transformation behavior appears independent of the cation site disproportionation behavior, showing no unusual feature at the special composition  $M'M_2''H(SeO_4)_2$ .

There has been recent discussion in the literature regarding the possible influence of strain on the superprotonic transition temperature in the  $M_3H(XO_4)_2$  class of compounds. In particular, Matuso et al.4 have suggested that spontaneous strain in the monoclinic phase, defined with respect to the dimensions of the trigonal phase, contributes to the formation energy of the former. The greater this strain, the lower the enthalpy of transition to the higher enthalpy trigonal phase, and consequently, the higher the transition temperature. Kiyanagi et al. 16 have suggested a more directly physical origin of strain energy as that deriving from the distortion of the selenate tetrahedra away from three-fold rotational symmetry about the Se-O bond. These authors suggest the standard deviation in O-Se-O angles as a metric for the strain. Because it is not possible to reliably determine oxygen coordinates in crystals with heavy elements from lab-based X-ray powder diffraction data, here, we consider the lattice parameter-based approach. In such cases, the transition temperature should follow the expression

$$T_{\rm sp} = C_1 - C_2 a_0^2 \tag{1}$$

where  $C_1$  and  $C_2$  are constants and the strain,  $a_0$ , is defined as

$$a_{\rm o} = \frac{b_{\rm m} - a_{\rm m}/\sqrt{3}}{2b_{\rm m}} \tag{2}$$

where  $a_{\rm m}$  and  $b_{\rm m}$  are the lattice constants in the monoclinic phase. In principle, these are the cell parameters at  $T_{\rm sp}$ , but the moderate transition temperatures imply thermal expansion effects are limited and the room-temperature lattice constants suffice for the analysis.

The measured transition temperatures are plotted in Figure 9 as a function of the square of the measured strain. The behavior suggests a correlation between these two parameters; however, the strain alone is not fully predictive of the transition temperature. In the  $(Cs_xRb_{1-x})_3H(SeO_4)_2$  system, the nonmonotonic behavior of the transition temperature with composition is reasonably well captured by the strain behavior, with Cs-rich and Rb-rich compositions of equal strain showing similar (within 10 °C) transition temperatures. However, with an overall variation in  $T_{\rm sp}$  of only 25 °C, a 10 °C difference at a given strain value is large and indicates the role of other factors. In the  $(K_xRb_{1-x})_3H(SeO_4)_2$  system, the results are strongly nonlinear. The transition temperature drops rather sharply between 0 and 50 at. % K, with a moderate decrease in  $a_0^2$ . Beyond 50 at. % K, the transition temperature is relatively unchanged despite a continued increase in  $a_0^2$ . Thus, although the data for Cs, Rb, and K compositions considered alone are almost co-linear, 20 the significant difference between the data of the solid solution systems brings into question models that suggest the transition temperature can be largely predicted by the global lattice strain. These solid solutions may serve as future model systems for evaluating more sophisticated analyses based on selenate group distortion.

**3.3. Transport Properties.** Beyond showing the occurrence of a phase transformation for all compositions, Figure 7 reveals that the magnitude of the conductivity in both chemical systems studied varies systematically with composition. In

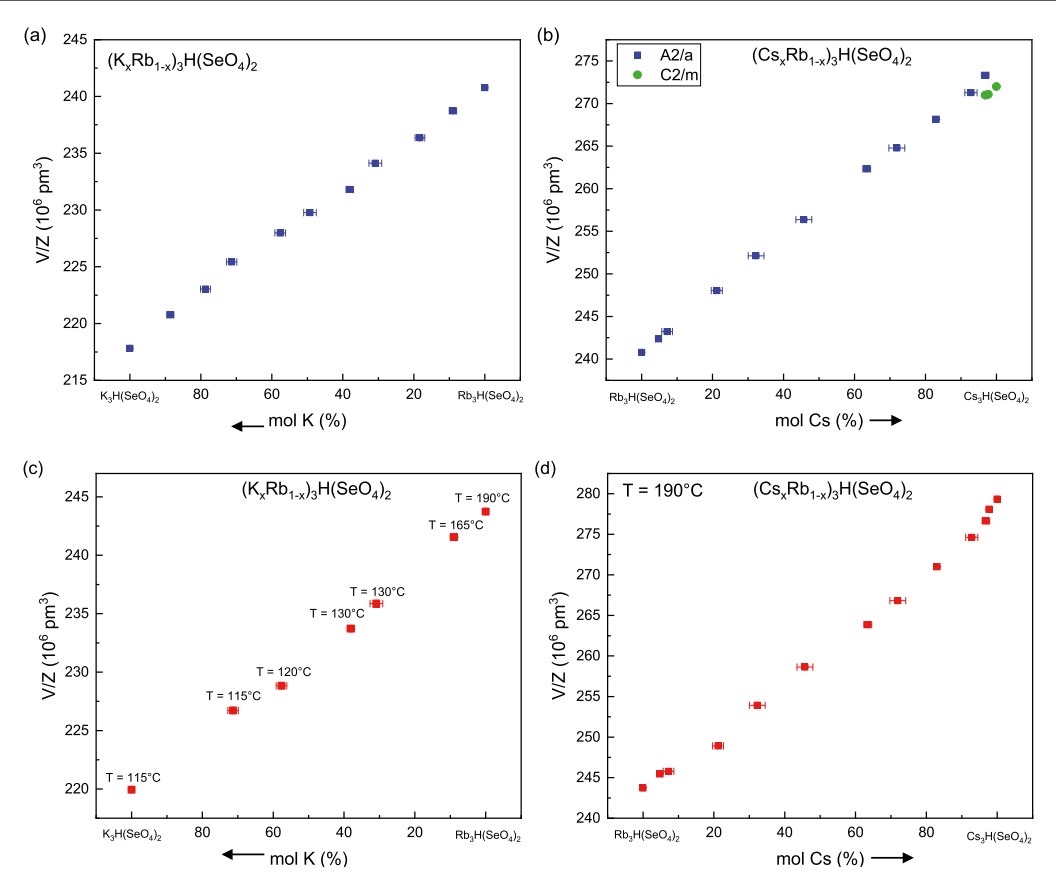


Figure 3. Molar volume of (a)  $(K_xRb_{1-x})_3H(SeO_4)_2$  and (b)  $(Cs_xRb_{1-x})_3H(SeO_4)_2$  materials at room temperature and, respectively, (c,d), at high temperatures under  $pH_2O \approx 0.023$  atm (balance  $N_2$  or He). In (c), data are reported for the  $(K_xRb_{1-x})_3H(SeO_4)_2$  system at a temperature a few degrees above the transition to the trigonal phases (as indicated), whereas in (d), data for the  $(Cs_xRb_{1-x})_3H(SeO_4)_2$  system are all at 190 °C. Molar volume error bars are obtained from uncertainty of the Rietveld fit and in most cases fall within the data points. Compositional error bars are obtained from EDS chemical analysis.

particular, in the superprotonic phase, the conductivity increases monotonically with decreasing cation ionic radius, Figure 10. Here, the conductivities measured at 190 °C for the  $(Cs_xRb_{1-x})_3H(SeO_4)_2$  materials are shown, along with extrapolated values for the  $(K_xRb_{1-x})_3H(SeO_4)_2$  materials. The latter is obtained, under the assumption of Arrhenius behavior in the superprotonic regime, eq 3

$$\sigma = \frac{A}{T} \exp\left(\frac{-E_{\rm a}}{k_{\rm B}T}\right) \tag{3}$$

where  $E_{\rm a}$  is the activation energy (formally, the activation enthalpy),  $k_{\rm B}$  is Boltzmann's constant, and A is the pre-exponential factor that includes the activation entropy.

Whether from the isotherm in Figure 10 or the complete conductivity data in Figure 7, it is evident that the K-rich materials display both high conductivity and a low superprotonic transition temperature. Accordingly, they have higher conductivity at lower temperatures than the Cs-rich materials have at higher temperatures. The beneficial impact of decreasing cation ionic radius observed here is, surprisingly, the opposite of what has been observed in  $Cs_{1-x}Rb_xH_2PO_4$ , in which introduction of Rb raises the transition temperature and decreases the superprotonic conductivity relative to neat  $CsH_2PO_4$ . In  $CsHSO_4$  as well, partial substitution Cs with Rb decreases the conductivity in the superprotonic phase, but in this case without significantly impacting the transition temperature. We speculate that in the  $M_3H(SeO_4)_2$ 

compounds, small cations may, as a consequence of contracting the structure, decrease the O–O hydrogen-bond distance and thereby decrease the barrier to proton transfer. Such an interpretation is supported by computational studies of  $Rb_3H(SeO_4)_2$  which suggest that proton transfer along the O–O bond is the rate-limiting step as opposed to selenate group reorientation. <sup>24</sup>

Consistent with the hypothesis that a decrease in cell volume and selenate-selenate interatomic distances may decrease the barrier to proton transport, the activation energies for transport, Figure 11, are found to decrease monotonically with decreasing cation size, with a possible anomaly in the vicinity of the special composition RbCs<sub>2</sub>H(SeO<sub>4</sub>)<sub>2</sub>. Shown also in Figure 11 is the pre-exponential factor, which is observed to vary with cation chemistry in a manner almost identical to that of the activation energy. The similarity in the trend lines motivates a direct comparison of the two quantities. As shown in Figure 12, ln(A) is approximately linearly related to the activation energy. Such a correlation, known as the Meyer-Neldel compensation rule, 25 has been observed in a wide range of materials and phenomena. Yelon and Movaghar have proposed that the behavior results from multiexcitation processes, which are required when the energy barrier for the process is large relative to  $k_{\rm B}T$  and thus to the typical excitations of the system. <sup>26</sup> Accessing these multiple excitation states implies a large configurational entropy, which then scales with the barrier energy. Linear scaling between ln(A) and  $E_a$ , as observed in the present study, is expected for most types of

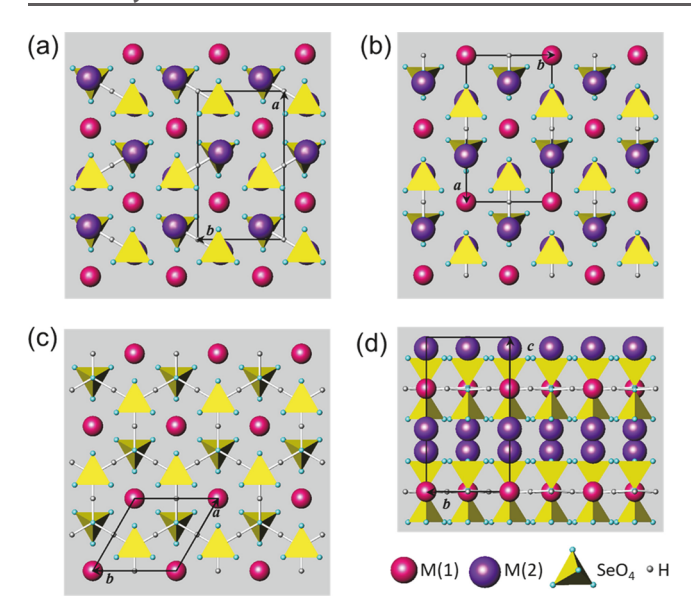


**Figure 4.** Crystal structures of  $M_3H(SeO_4)_2$  solid acids: (a) room-temperature A2/a monoclinic structure of  $K_3H(SeO_4)_2$  and  $Rb_3H(SeO_4)_2$  shown in projection on (001); (b) room-temperature C2/m monoclinic structure of  $Cs_3H(SeO_4)_2$  at room temperature shown in projection on (001); (c) high-temperature  $R\overline{3}m$  structure of all three  $M_3H(SeO_4)_2$  compounds (M=K, Rb, Cs), shown in projection on (001); (d) high-temperature  $R\overline{3}m$  structure shown in projection on (100). For simplicity, only portions of the structure along the (001\*) direction are shown. In addition, hydrogen atoms are placed on high symmetry sites and partial occupancies are not indicated.

excitations. The slope of  $\ln(A)$  versus  $E_{\rm a}$  in such cases is equal to  $1/\Delta_0$ , where  $\Delta_0$  is the energy scale of the excitations and  $T_0 = \Delta_0/k_{\rm B}$  is the isokinetic temperature, the temperature at which all materials in the class have the same value of the property of interest; here, conductivity.

The data in Figure 12 reveal three distinct regions of behavior. The compounds in the  $(K_xRb_{1-x})_3H(SeO_4)_2$  system are described by a single linear correlation, whereas those in the  $(C_xRb_{1-x})_3H(SeO_4)_2$  system are described by two lines with slightly differing slopes but experimentally identical intercepts. The resulting three  $\Delta_0$  values lie between about 55 and 80 meV. In the superprotonic phases of these materials,

all protons are understood to participate in the transport process. Consequently, defect formation energies do not contribute to  $E_a$  and cannot explain the distinct values of  $\Delta_0$ . This stands in contrast to a recent study of Li-ion conductors, in which scatter in the Meyer-Neldel plot could be resolved by considering defect formation energies.<sup>27</sup> Instead, here, microscopic chemical factors may generate different excitation processes across the  $(K_xRb_{1-x})_3H(SeO_4)_2$  and  $(Cs_xRb_{1-x})_3H$ -(SeO<sub>4</sub>)<sub>2</sub> systems. Such factors may also explain the different intercept values, which reflect terms such as jump distance and attempt frequency. The measurable change in  $\Delta_0$  at the special composition of  $Cs_2RbH(SeO_4)_2$  in the  $(Cs_xRb_{1-x})_3H(SeO_4)_2$ system points toward an influence of the cation distributions over the M(1) and M(2) sites in the  $R\overline{3}m$  phase on the energetics of proton transport. There is a hint of a similar effect in the  $(K_xRb_{1-x})_3H(SeO_4)_2$  system, but the evidence is less convincing.

## 4. SUMMARY AND CONCLUSIONS

On the basis of X-ray diffraction and conductivity studies, the phase diagrams of the  $(K_xRb_{1-x})_3H(SeO_4)_2$  and  $(Cs_xRb_{1-x})_3H(SeO_4)_2$  systems have been established.  $K_3H$ -(SeO<sub>4</sub>)<sub>2</sub> and Rb<sub>3</sub>H(SeO<sub>4</sub>)<sub>2</sub> are completely miscible at room temperature, with all compositions crystallizing with the monoclinic structure in space group A2/a. In the  $(Cs_xRb_{1-x})_3H(SeO_4)_2$  system, in which the distinct structures of the end-members preclude complete miscibility at ambient temperature, it is found that Cs is highly soluble in  $Rb_3H(SeO_4)_2$ , with the A2/a monoclinic phase occurring at compositions up to 93 at. % Cs. Conversely, the solubility of Rb into the C2/m structure of  $Cs_3H(SeO_4)_2$  is only  $\sim 2$  at. %. At 97% Cs, a two-phase mixture of both the  $Rb_3H(SeO_4)_2$  and  $Cs_3H(SeO_4)_2$  structure types occurs. Furthermore, in both systems, there is a preference for larger cations to be incorporated at sites between the  $H(SeO_4)_2$  layers rather than sites within the layers.

All compositions undergo a superprotonic transition to the trigonal R3m phase well-known for the  $M_3H(SeO_4)_2$  class of solid acids. All two-phase regions are narrow, suggesting that the thermodynamics of mixing are the same across crystal structures, consistent with the observation that site occupancies are unchanged across the transition. Significantly, both

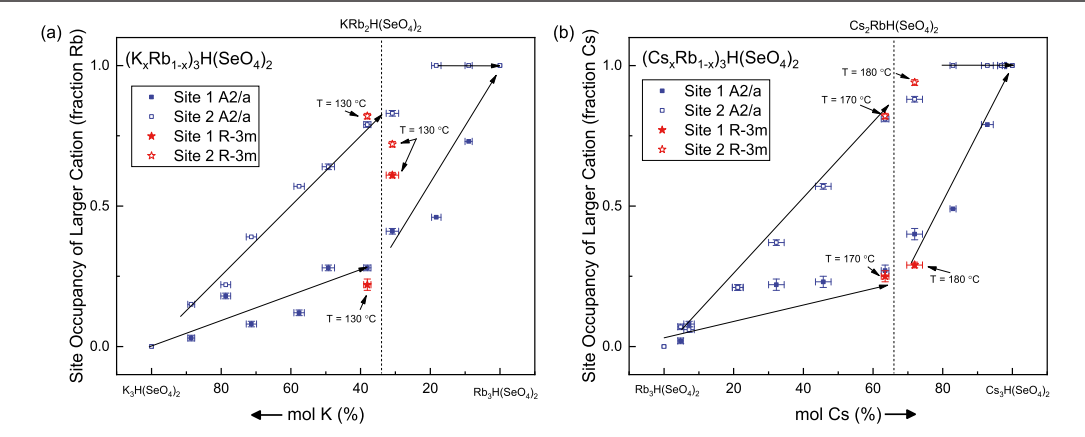


Figure 5. Site occupancies in (a)  $(K_xRb_{1-x})_3H(SeO_4)_2$  and (b)  $(Cs_xRb_{1-x})_3H(SeO_4)_2$  solid solutions in the room temperature and high-temperature phases (as indicated). Arrows on each figure are guide to the eye, indicating trends. The vertical dashed lines indicate the special compositions  $KRb_2H(SeO_4)_2$  and  $Cs_2RbH(SeO_4)_2$ , respectively. These compositions correspond to those in which cations sites are fully differentiated, and the larger cation resides in the larger of the two available cation sites. Site occupancy error bars are obtained from uncertainty of the Rietveld fit, and compositional error bars are obtained from EDS chemical analysis.

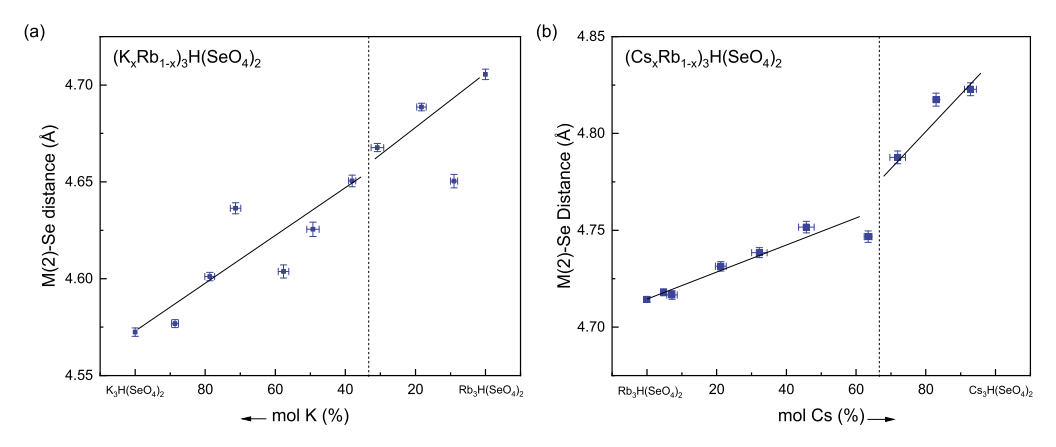


Figure 6. Distance between M(2) and Se atoms (at room temperature) along the pseudotrigonal axis in (a)  $(K_xRb_{1-x})_3H(SeO_4)_2$  (a) and (b)  $(Cs_xRb_{1-x})_3H(SeO_4)_2$ . Lines on each figure are drawn to help the eye and indicate trends. The vertical dashed lines indicate the special compositions  $KRb_2H(SeO_4)_2$  and  $Cs_2RbH(SeO_4)_2$ , respectively. M(2)-Se distance error bars are obtained from uncertainty of the Rietveld fit, and compositional error bars are obtained from EDS chemical analysis.

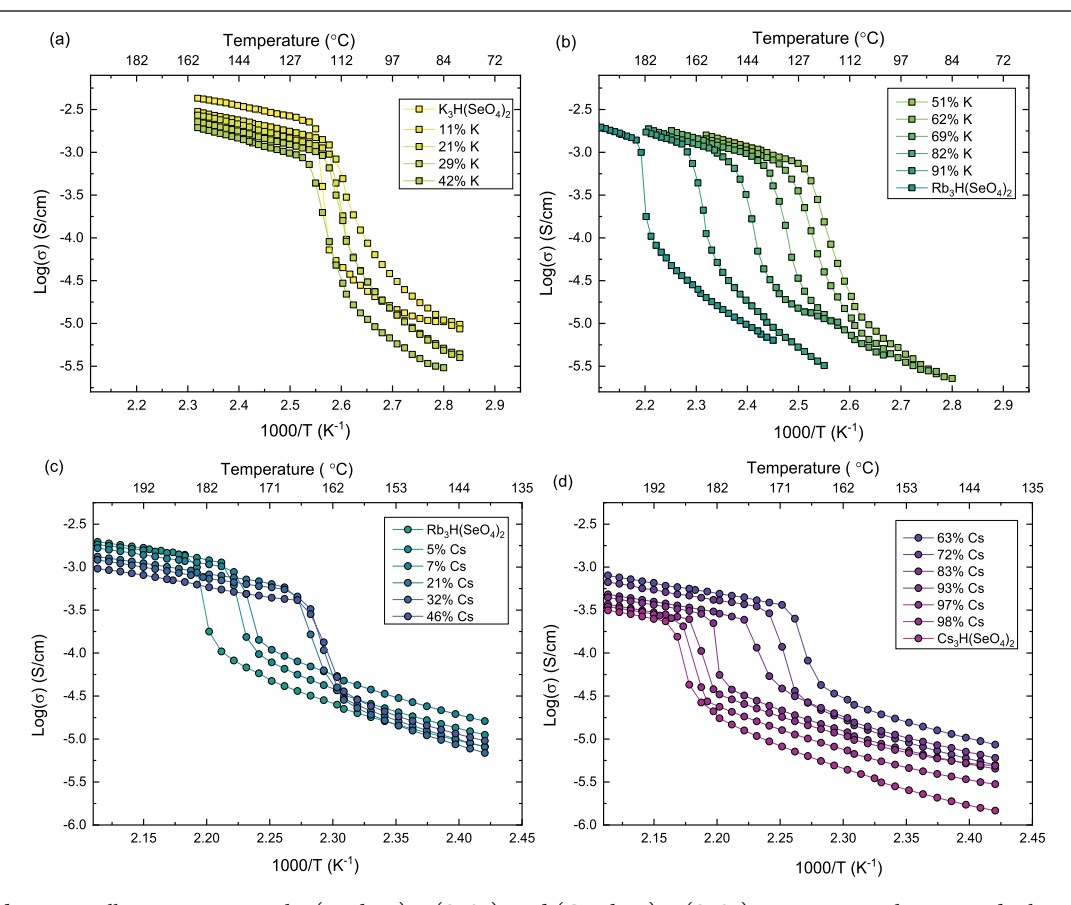


Figure 7. Conductivities all compositions in the  $(K_xRb_{1-x})_3H(SeO_4)_2$  and  $(Cs_xRb_{1-x})_3H(SeO_4)_2$  systems upon heating under humidified nitrogen  $(pH_2O\approx 0.473 \text{ atm})$ : (a) 100-58% K, (b) 49-0% K, (c) 0-46% Cs, and (d) 63-100% Cs.

systems show a minimum in the superprotonic transition temperature, with a  $T_{\rm sp}$  that is loosely correlated with the magnitude of the strain of the monoclinic phase relative to the ideal trigonal structure. The correlation suggests that distortion of the selenate group away from the ideal three-fold symmetry about the apical oxygen atom increases the formation energy of the monoclinic phase and lowers the enthalpic driving force for the superprotonic transition. Overall, the transition temperatures in the  $(K_xRb_{1-x})_3H(SeO_4)_2$  system are significantly below those of the  $(Cs_xRb_{1-x})_3H(SeO_4)_2$  system. Furthermore, there is a monotonic increase in superprotonic

conductivity and a monotonic decrease in activation energy with decreasing average cation ionic radius. This behavior is tentatively attributed to a contraction in the length of the hydrogen bonds, presumed from the contraction of the cell volume. At high temperatures, there is also a clear correlation between activity energy and pre-exponential factor for proton transport. Overall, the systematic variation of chemical and crystallographic properties in the  $(K_xRb_{1-x})_3H(SeO_4)_2$  and  $(Cs_xRb_{1-x})_3H(SeO_4)_2$  systems provide an ideal test bed from which the factors controlling superprotonic transport can be

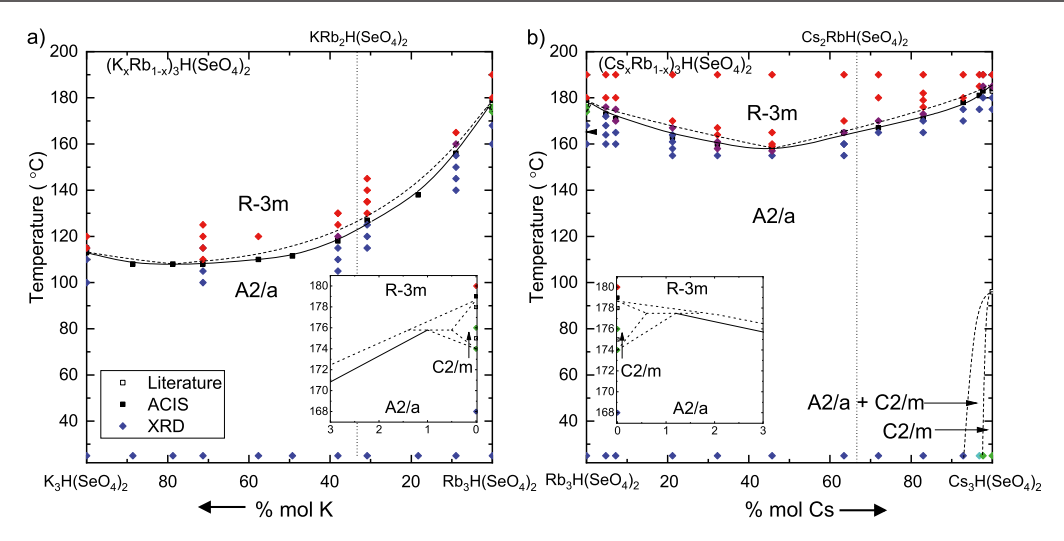
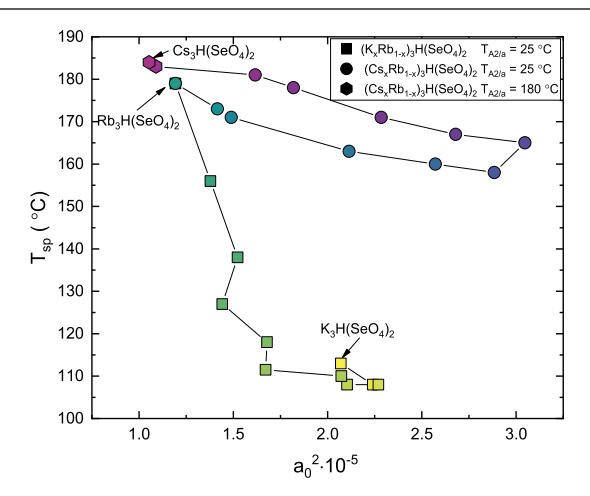
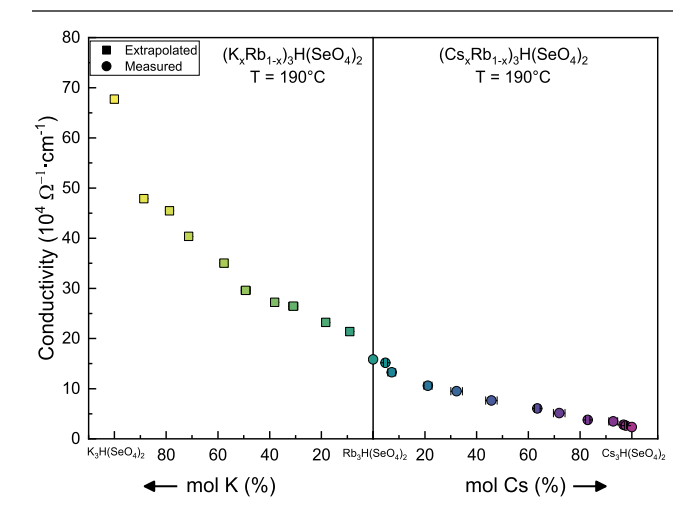


Figure 8. Phase diagrams of the  $(M_xRb_{1-x})_3H(SeO_4)_2$  systems: (a)  $(K_xRb_{1-x})_3H(SeO_4)_2$  and (b)  $(Cs_xRb_{1-x})_3H(SeO_4)_2$ .



**Figure 9.** Superprotonic transition temperature  $(T_{\rm sp})$  vs  $a_0^2$  in the  $(C_{\rm s}_xRb_{1-x})_3H(SeO_4)_2$  and  $(K_xRb_{1-x})_3H(SeO_4)_2$  systems. The 98 and 100% Cs values were calculated using the lattice parameter of the A2/a phase at 180 °C. The color of the data points correspond to the compositions as given in Figure 7. The uncertainty in the  $a_0^2$  is smaller than the size of the symbols.



**Figure 10.** Isothermal conductivities of  $(K_xRb_{1-x})_3H(SeO_4)_2$  and  $(Cs_xRb_{1-x})_3H(SeO_4)_2$  at 190 °C. Conductivities of  $(K_xRb_{1-x})_3H(SeO_4)_2$  are extrapolated assuming Arrhenius behavior, eq 3, whereas conductivities of  $(Cs_xRb_{1-x})_3H(SeO_4)_2$  are measured.

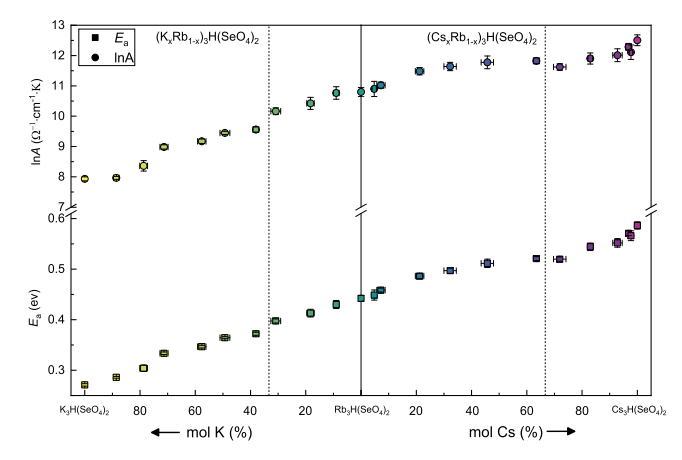


**Figure 11.** Activation energy and pre-exponential factor of conductivity in the  $(K_xRb_{1-x})_3H(SeO_4)_2$  and  $(Cs_xRb_{1-x})_3H(SeO_4)_2$  systems as functions of composition.

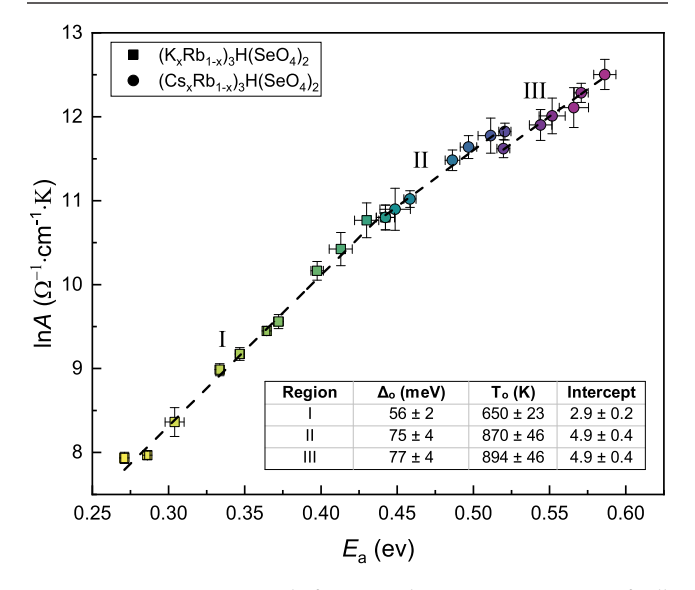


**Figure 12.** Pre-exponential factor and activation energy of all compositions presented in a Meyer–Neldel plot. The color of the data points correspond to the compositions as given in Figure 7.

established. The studies carried out here are an important step on that path.

## ASSOCIATED CONTENT

## Supporting Information

The Supporting Information is available free of charge on the ACS Publications website at DOI: 10.1021/acs.chemmater.9b03856.

Synthesis details, chemical analysis, X-ray diffraction analysis, Rietveld refinement parameters, measured compositions of  $(K_xRb_{1-x})_3H(SeO_4)_2$  and  $(Cs_xRb_{1-x})_3H(SeO_4)_2$  solid solutions determined using EDS, experimental and simulated room-temperature diffraction patterns after Rietveld refinement, percentage change in room-temperature linear dimensions in  $(K_x Rb_{1-x})_3 H(SeO_4)_2$  and  $(Cs_x Rb_{1-x})_3 H(SeO_4)_2$  as a function of composition, coordination polyhedra of  $(K_xRb_{1-x})_3H(SeO_4)_2$  and  $(Cs_xRb_{1-x})_3H(SeO_4)_2$  solid solutions at room temperature, select atomic coordinates of  $(K_xRb_{1-x})_3H(SeO_4)_2$  and  $(Cs_xRb_{1-x})_3H(SeO_4)_2$  solid solutions at room temperature, refined lattice parameters and site occupancies of the  $R\overline{3}m$  phase of  $(K_xRb_{1-x})_3H$ - $(SeO_4)_2$  and  $(Cs_rRb_{1-r})_3H(SeO_4)_2$  solid solutions at high temperatures, alternating current impedance spectroscopy, onset and final temperatures of the superprotonic transition as measured by ACIS, and selected impedance spectra of Rb<sub>3</sub>H(SeO<sub>4</sub>)<sub>2</sub> (PDF)

## AUTHOR INFORMATION

## **Corresponding Author**

\*E-mail: sossina.haile@northwestern.edu.

ORCID 6

Dezhi Yi: 0000-0002-6374-706X Sheel Sanghvi: 0000-0002-9962-3587

Chatr Panithipongwut Kowalski: 0000-0001-8807-815X

Sossina M. Haile: 0000-0002-5293-6252

#### Notes

The authors declare no competing financial interest. <sup>#</sup>Equal first authors.

## ACKNOWLEDGMENTS

Financial support has been provided by National Science Foundation (DMR 1807234) and the Ministry of Science and Technology of Thailand through the Royal Thai Scholarship. This work made use of the Jerome B. Cohen X-Ray Diffraction Facility supported by the MRSEC program of the National Science Foundation (DMR-1720139) at the Materials Research Center of Northwestern University and the Soft and Hybrid Nanotechnology Experimental (SHyNE) Resource (NSF ECCS-1542205.) This work additionally made use of the IMSERC at Northwestern University, which has also received support from the Soft and Hybrid Nanotechnology Experimental (SHyNE) Resource (NSF ECCS-1542205), as well as the State of Illinois and the International Institute for Nanotechnology (IIN). This study was initiated at the California Institute of Technology which is also gratefully acknowledged.

## REFERENCES

(1) Shikanai, F.; Tomiyasu, K.; Kiyanagi, R.; Yonemura, M.; Iwase, K.; Sulistyanintyas, D.; Wurnisha, T.; Mori, K.; Ishigaki, T.; Tsukushi,

I.; Ikeda, S.; Kamiyama, T. Neutron Powder Diffraction Study of Protonic Conductor K<sub>3</sub>H(SeO<sub>4</sub>)<sub>2</sub>. Ferroelectrics **2007**, 347, 74–78.

- (2) Merinov, B.; Haile, S. M.; Bismayer, U. Crystal structure of the "intermediate" phase of the protonic conductor Rb<sub>3</sub>H(SeO<sub>4</sub>)<sub>2</sub>. Solid State Ionics **2002**, 146, 355–365.
- (3) Dilanyan, R. A.; Sinitsyn, V. V.; Shekhtman, V. S.; Baranov, A. I.; Shuvalov, L. A. The Discovery of an Intermediate Phase between the Low-Conducting and Super-Protonic Phases in Rb<sub>3</sub>H(SeO<sub>4</sub>)<sub>2</sub> Crystal. *Kristallografiya* **1994**, *39*, 484–487.
- (4) Matsuo, Y.; Tanaka, Y.; Hatori, J.; Ikehata, S. Proton activity and spontaneous strain of  $Cs_3H(SeO_4)_2$  in the phase transition at 369 K. *Solid State Commun.* **2005**, 134, 361–365.
- (5) Merinov, B. V.; Baranov, A. I.; Shuvalov, L. A. Crystal-Structure and Mechanism of Protonic Conductivity of a Superionic Phase of Cs<sub>3</sub>H(SeO<sub>4</sub>)<sub>2</sub>. *Kristallografiya* **1990**, *35*, 355–360.
- (6) Merinov, B. V.; Bolotina, N. B.; Baranov, A. I.; Shuvalov, L. A. Crystal-Structure of  $Cs_3H(SeO_4)_2$  (T = 295K) and its Modifications under Phase-Transitions. *Kristallografiya* **1988**, 33, 1387–1392.
- (7) Merinov, B. V.; Bolotina, N. B.; Baranov, A. I.; Shuvalov, L. A. Crystal-Structure of a Ferroelastic Phase-II of Cs<sub>3</sub>H(SeO<sub>4</sub>)<sub>2</sub>. *Kristallografiya* **1991**, *36*, 1131–1134.
- (8) Sonntag, R.; Melzer, R.; Wessels, T.; Radaelli, P. G. Cs<sub>3</sub>H(SeO<sub>4</sub>)<sub>2</sub> at 300 K by high-resolution neutron powder diffraction. Acta Crystallogr., Sect. C: Cryst. Struct. Commun. 1997, 53, 1529–1531
- (9) Komukae, M.; Sakata, K.; Osaka, T.; Makita, Y. Optical and X-ray Studies in Ferroelastic Cs<sub>3</sub>H(SeO<sub>4</sub>)<sub>2</sub>. J. Phys. Soc. Jpn. **1994**, 63, 1009–1017.
- (10) Ichikawa, M.; Gustafsson, T.; Olovsson, I. Structure and nature of the low-temperature phase transition in  $M_3H(XO_4)_2$ -type crystals with a zero-dimensional H-bond network. *J. Mol. Struct.* **1994**, 321, 21–23.
- (11) Kirpichnikova, L.; Hilczer, B.; Polomska, M.; Szczesniak, L.; Pawlowski, A. Ferroelastic domain structure and thermal behavior of some  $Me_3H(XO_4)_2$  crystals in the vicinity of superprotonic phase transitions. *Solid State Ionics* **2001**, *145*, 191–196.
- (12) Pawłowski, A.; Polomska, M.; Hilczer, B.; Szczesniak, L.; Pietraszko, A. Superionic phase transition in Rb<sub>3</sub>D(SeO<sub>4</sub>)<sub>2</sub> single crystals. *J. Power Sources* **2007**, *173*, 781–787.
- (13) Pawlowski, A.; Szczesniak, L.; Polomska, M.; Hilczer, B.; Kirpichnikova, L. Pretransitional effects at the superionic phase transition of Rb<sub>3</sub>H(SeO<sub>4</sub>)<sub>2</sub> protonic conductor. *Solid State Ionics* **2003**, *157*, 203–208.
- (14) Chen, R. H.; Chang, R. Y.; Shern, S. C. Dielectric and AC ionic conductivity investigations in  $K_3H(SeO_4)_2$  single crystal. *J. Phys. Chem. Solids* **2002**, *63*, 2069–2077.
- (15) Melzer, R. The structure of the proton conducting phase of Rb<sub>3</sub>H(SeO<sub>4</sub>)<sub>2</sub> at 470 K. Solid State Ionics **1996**, 92, 119–127.
- (16) Kiyanagi, R.; Matsuo, Y.; Ohhara, T.; Kawasaki, T.; Oikawa, K.; Kaneko, K.; Tamura, I.; Hanashima, T.; Munakata, K.; Nakao, A.; Kawakita, Y., Phase Transition and Internal Crystal Structure of Superprotonic Conductor, Rb<sub>3-x</sub>K<sub>x</sub>H(SeO<sub>4</sub>)<sub>2</sub>. Proceedings of the 2nd International Symposium on Science at J-PARC, 2015; Vol. 8.
- (17) Toby, B. H.; Von Dreele, R. B. GSAS-II: the genesis of a modern open-source all purpose crystallography software package. *J. Appl. Crystallogr.* **2013**, *46*, 544–549.
- (18) Schwalbe, C. H. Lars Vegard: key communicator and pioneer crystallographer. *Crystallogr. Rev.* **2014**, *20*, 9–24.
- (19) Ikeda, A.; Kitchaev, D. A.; Haile, S. M. Phase behavior and superprotonic conductivity in the Cs<sub>1-x</sub>Rb<sub>x</sub>H<sub>2</sub>PO<sub>4</sub> and Cs<sub>1-x</sub>K<sub>x</sub>H<sub>2</sub>PO<sub>4</sub> systems. *J. Mater. Chem. A* **2014**, *2*, 204–214.
- (20) Matsuo, Y.; Hatori, J.; Kamazawa, K.; Sugiyama, J.; Yoshida, Y.; Ikehata, S. Scaling of superionic transition temperature in  $M_3D$ - $(XO_4)_2$ . Solid State Ionics **2012**, 225, 40–42.
- (21) Mhiri, T.; Colomban, P. Defect-Induced Smoothing of the Superionic Phase-Transition in Cs<sub>1-x</sub>M<sub>x</sub>HSO<sub>4</sub> Protonic Conductors. III. *Solid State Ionics* **1991**, *44*, 235–243.

(22) Merinov, B. V.; Jones, D. J.; Rozière, J.; Mhiri, T. Mixed alkali metal sulfate proton conductors: The structure of  $Cs_{0.9}Rb_{0.1}HSO_4$  at room temperature. *Solid State Ionics* **1996**, *91*, 323–330.

- (23) Kreuer, K.-D. Proton Conductivity: Materials and Applications. *Chem. Mater.* **1996**, *8*, 610–641.
- (24) Pavlenko, N.; Pietraszko, A.; Pawlowski, A.; Polomska, M.; Stasyuk, I. V.; Hilczer, B. Hydrogen transport in superionic system Rb<sub>3</sub>H(SeO<sub>4</sub>)<sub>2</sub>: A revised cooperative migration mechanism. *Phys. Rev. B: Condens. Matter Mater. Phys.* **2011**, *84*, 064303.
- (25) Meyer, W.; Neldel, H. Relation Between the Energy Constant E and the Quantity Constant a in the Conductivity-Temperature Formula for Oxide Semiconductors. Z. Tech. Phys. 1937, 18, 588–593
- (26) Yelon, A.; Movaghar, B. Microscopic explanation of the compensation (Meyer-Neldel) rule. *Phys. Rev. Lett.* **1990**, *65*, 618–620
- (27) Muy, S.; Bachman, J. C.; Chang, H.-H.; Giordano, L.; Maglia, F.; Lupart, S.; Lamp, P.; Zeier, W. G.; Shao-Horn, Y. Lithium Conductivity and Meyer-Neldel Rule in Li<sub>3</sub>PO<sub>4</sub>–Li<sub>3</sub>VO<sub>4</sub>–Li<sub>4</sub>GeO<sub>4</sub> Lithium Superionic Conductors. *Chem. Mater.* **2018**, *30*, 5573–5582.